RESEARCH ARTICLE

Research on wearable electrochemical sensors for real-time monitoring of antiepileptic drug plasma concentrations for precision medicine

Ting Ding*

School of Biological Medicine, Changjiang Polytechnic, Wuhan, Hubei, China.

Received: March 26, 2026; **accepted:** June 16, 2026.

Antiepileptic therapy requires timely control of plasma drug concentrations because underexposure may reduce seizure suppression and overexposure may increase adverse reactions, while conventional therapeutic drug monitoring still depends largely on delayed offline assays. This study developed a wearable electrochemical sensing system for real-time monitoring of antiepileptic drug plasma concentrations and to support precision medicine-oriented dose adjustment under continuous low-concentration and interference-prone body-fluid monitoring scenarios during long-term wearable detection processes. The design also addressed delayed sampling, signal drift, and body-fluid-to-plasma mapping limitations found in current monitoring approaches. The system integrated a flexible three-electrode platform, microfluidic sampling channels, and a reduced graphene oxide/gold nanoparticles/molecularly imprinted polymer functional layer. The differential pulse voltammetry (DPV) with a multi-feature fusion regression model was used for concentration inversion and dynamic correction. The sensor showed a linear response within 0.05 – 10 µmol/L with a detection limit of 0.03 µmol/L. Under interference-resistant conditions, the response deviation remained below 8%, and the correlation coefficient with the standard method exceeded 0.98. These results indicated that the proposed system provided sensitive, stable, and real-time plasma concentration monitoring, offering a feasible technical route for individualized dosing of antiepileptic medications and clinical precision medicine applications.

Keywords: wearable sensor; electrochemical detection; antiepileptic drugs; molecular imprinting; plasma concentration; precision dosing.

***Corresponding author:** Ting Ding, School of Biological Medicine, Changjiang Polytechnic, Wuhan, Hubei 430074, China. Email: si_maidou@163.com.

Introduction

Antiepileptic drug therapy depends on maintaining plasma concentrations within a narrow therapeutic window because insufficient exposure may fail to suppress seizures whereas excessive exposure may increase adverse reactions and reduce long-term treatment adherence. Therefore, real-time and patient-adaptive monitoring of antiepileptic drug plasma concentrations has become an important scientific requirement in precision medicine and individualized epilepsy management. Existing studies have shown that biosensor technology has gradually emerged as a promising route for antiepileptic drug analysis because electrochemical platforms can provide high sensitivity, rapid response, and miniaturization potential for therapeutic monitoring [1].

Wearable devices have also progressed from physiological signal acquisition to continuous health surveillance including real-time seizure detection and neurological status tracking, which

creates a technical basis for integrating drug monitoring into body-worn systems [2]. Research on wearable and implantable continuous drug monitoring has further demonstrated that miniaturized sensors can support sustained biochemical observation in complex biological environments, which is highly relevant to individualized pharmacotherapy [3]. Recent work in precision medicine has also emphasized the role of wearable sensors in therapeutic drug monitoring and personalized dosing, indicating a clear trend from static measurement toward continuous and decision-oriented monitoring [4]. In parallel, the combination of nanomaterials, artificial intelligence, and wearable technology has significantly improved electrochemical biosensor performance in terms of selectivity, signal amplification, and practical deployment, expanding the translational value of such systems from laboratory validation to real-world application scenarios [5]. More broadly, electrochemical biosensors are increasingly regarded as an enabling nexus for precision medicine because they support decentralized testing, rapid biochemical feedback, and closer coupling between diagnosis and treatment adjustment [6]. However, several urgent issues still restrict the practical application of wearable antiepileptic drug monitoring. Reliable sensing of pharmaceutical molecules in complex biofluids remains difficult when endogenous interferents, nonspecific adsorption, environmental fluctuation, and matrix-induced signal distortion jointly affect sensor output [7]. Furthermore, the rise of wearable and implantable biosensors in closed-loop therapeutic systems has highlighted the growing demand for integrated platforms that not only detect biochemical changes continuously but also provide data robust enough for therapeutic decision support [8]. In the specific context of antiepileptic drug monitoring, most existing methods still depend on offline sampling and laboratory analysis. Real-time tracking of drug concentration variation in body fluids is insufficient. The stable correlation between peripheral body-fluid signals and actual plasma concentration has not been fully established. The synergistic optimization of sensing materials, flexible device structures, microfluidic sampling, and signal-processing models remain inadequate.

This study aimed to develop a wearable electrochemical sensing system for real-time monitoring of antiepileptic drug plasma concentrations and to improve its applicability to precision medicine-oriented dose adjustment. The study adopted a combined methodological framework involving a flexible three-electrode platform, a microfluidic sampling structure, a reduced graphene oxide/gold nanoparticles/molecularly imprinted composite functional layer for selective recognition and signal enhancement, differential pulse voltammetry (DPV) for electrochemical acquisition, and a multi-feature fusion model for concentration inversion and dynamic correction. Through this integrated strategy, the work sought to enhance sensitivity, selectivity, stability, and quantitative reliability under low-concentration and interference-prone body-fluid conditions. This research provided a technically coherent route toward continuous therapeutic drug monitoring for epilepsy management and in supporting the scientific development of wearable electrochemical biosensing, closed-loop medication support, and precision medicine-oriented sensing systems.

Materials and methods

Electrochemical detection mechanism

Electron-transfer active groups and their adsorption characteristics at the electrode interface determine their electrochemical detectability of antiepileptic drugs. Representative antiepileptic drugs such as carbamazepine and lamotrigine contain aromatic conjugated structures, amino groups, or amide groups that can be oxidized under an applied potential and generate characteristic voltammetric peaks. Differences in molecular orbital energy, polarity, and dissociation behavior lead to variations in peak potential, current intensity, and reaction reversibility. The

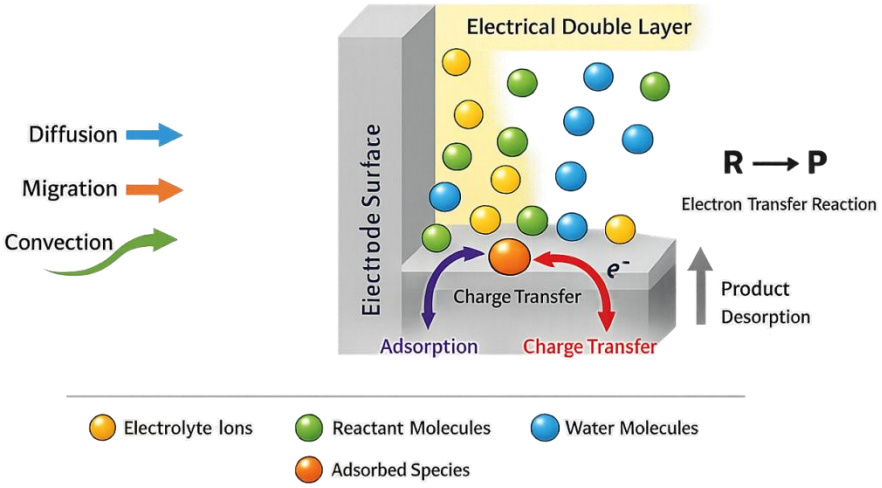

Figure 1. Schematic diagram of mass transfer–adsorption–charge transfer mechanisms at the electrode interface.

dissociation state of small drug molecules is affected by pH, ionic strength, and protein adsorption, while interfacial mass-transfer resistance weakens the effective response of free drug molecules in biological fluids. Thus, wearable detection must focus on targets that have a well-defined electroactive window, low protein-binding interference, and high interfacial enrichment potential. Meanwhile, the electrode materials must be able to control the local electron density and adsorption energy to develop better sensitivity to current response at low-concentration conditions. In this study, the response of the antiepileptics at the wearable sensor interface was successively divided into three phases including the body-fluid mass transfer, the surface adsorption, and the electric charge transfer (Figure 1). After the drug entered the diffusion layer from the microfluidic channel, it first satisfied the diffusion flux relationship as below.

$$J = -D\frac{\partial C}{\partial x} \quad (1)$$

where *J* was the mass transfer flux per unit area. *D* was the diffusion coefficient. *C* was the drug concentration. *x* was the diffusion distance. Molecules reaching the electrode surface underwent further adsorption, and their coverage was expressed as follows.

$$\theta = \frac{KC}{1+KC} \quad (2)$$

where θ was the surface coverage. *K* was the adsorption equilibrium constant. The interfacial charge transfer rate followed the Butler-Volmer relationship as follows.

$$i = i_0\left[exp\left(\frac{\alpha nF\eta}{RT}\right) - exp\left(-\frac{(1-\alpha)nF\eta}{RT}\right)\right] \quad (3)$$

where i was the reaction current. i_0 was the exchange current density. α was the charge transfer coefficient. *n* was the number of electrons transferred. *F* was the Faraday constant. η was the overpotential. *R* was the gas constant. *T* was the absolute temperature. In wearable applications, the surface roughness of the flexible electrode and the density of active sites in the functional layer jointly determined *K* and i_0, while microfluidic transport conditions primarily affected *D* and the thickness of the diffusion layer [9, 10]. Thus, to obtain a stable and distinct voltammetric response in low concentration body fluid environment, it was necessary for the design of the interface kinetic model to optimize the mass transfer path, the adsorption enrichment capacity, and the electron exchange rate. The wearable electrochemical detection of antiepileptic drugs, uric acid, ascorbic acid, lactic acid, glucose, and inorganic ions in sweat or interstitial fluid might cause peak

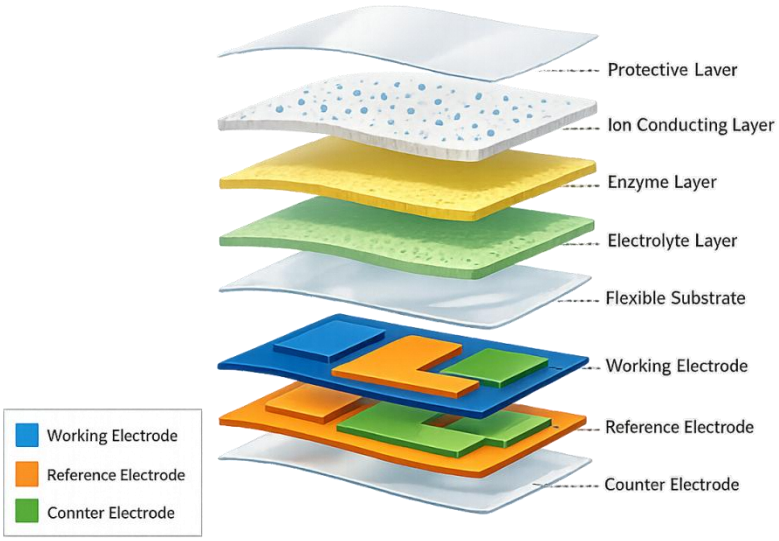

Figure 2. Schematic of the flexible three-electrode structure and functional layer distribution.

overlap, elevated background current, and competitive interfacial adsorption, thereby distorting the target drug signal. The selective recognition mechanism design should center on the principle of material screening - interface recognition - signal discrimination. The molecularly imprinted polymer or functionalized nanocomposite layer should be fabricated over the working electrode surface to further improve the preferential enrichment of target molecules in terms of their cavity matching and local charge interaction. The thickness, surface polarity and pore-size distribution of the modified layer needed to be controlled to suppress the macromolecular contamination and nonspecific adsorption. DPV-based signal discrimination and multi-parameter compensation should be combined to improve the reliability of concentration inversion. During continuous monitoring, temperature, pH, and ionic-strength compensation terms should also be introduced to reduce the influence of body-fluid environmental changes on selective recognition stability and ensure reproducible inputs for subsequent concentration inversion.

Flexible electrode and functional material construction

The flexible three-electrode assembly adopted a layered structure consisting of a polyimide substrate, conductive interconnection layer, functional sensing layer, ion-selective protective layer, and biocompatible encapsulation layer (Figure 2). The substrate was fitted with thickness of 25 μm. An oxygen plasma activation period of 60 s was experienced, after which a 5 nm Ti layer and a 120 nm Au layer were deposited to provide the interconnections. The working electrode diameter was set to 2.5 mm, the reference electrode was printed Ag/AgCl, and the counter electrode was designed as a serpentine Ag/Au mesh to reduce stress concentration during bending. The bending stability of conductivity was determined below.

$$\frac{\Delta R}{R_0} = k\varepsilon \quad (4)$$

where ΔR was the change in resistance. R_0 was the initial resistance. k was the strain sensitivity coefficient. ε was the surface strain. By setting the serpentine line width to 80 μm and the radius of curvature to 150 μm, ε was confined to the low-strain region [11, 12]. The working electrode functional layer was constructed in three steps using reduced graphene oxide/gold nanoparticles/molecularly imprinted polymer. 4 μL of 2 mg/mL reduced graphene oxide

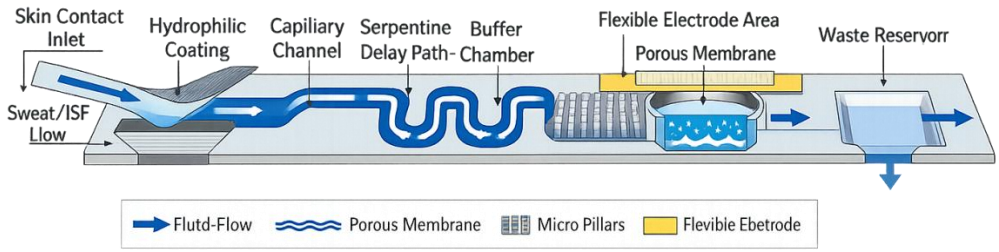

Figure 3. Schematic diagram of the microfluidic sampling channel.

dispersion was spot-coated followed by the electrodeposition of 20 – 35 nm Au nanoparticles at a potential of −0.20 V for 180 s. The thickness of the imprinting layer was determined below.

$$\delta = \frac{QM}{nF\rho A} \quad (5)$$

where δ was the polymer layer thickness. Q was the polymer charge. *M* was the polymer molar mass. *n* was the number of electron transfers. *F* was the Faraday constant. ρ was the material density. *A* was the electrode area. The electro-polymerization charge was controlled to 8 - 12 mC/cm^2 to allow the formation of recognition holes without excessively blocking electron transport. A 1.5 µm porous polyurethane protection film was applied to the outer layer to limit the high molecular pollution and keep the fluid diffusion flux.

Microfluidic and body fluid sampling design

A series structure of microfluidic sampling layer comprising of a series of skin-contact inlet, capillary-based main channel, flow-stabilizing buffer chamber, detection chamber, waste collection channel was incorporated and in line with the flexible three-electrode working space (Figure 3). Polydimethylsiloxane substrate was applied with 200 µm thick, 120 - 180 µm, and channel height of 35 - 60 µm to maintain an effective volume of the detecting chamber between 0.8 - 1.5 µL [13]. Conical convergence channel and a hydrophilic modified layer were positioned on the side of the inlet whereby the angle of contact had been regulated at 25 - 35°. Capillary pressure differences were utilized to drive sweat or trace amounts of interstitial fluid into the main channel in a directed manner with the driving force satisfying the following.

$$\Delta P = \frac{2\gamma \cos\theta}{r_{eq}} \quad (6)$$

where ΔP was the capillary pressure difference. γ was the liquid surface tension. θ was the contact angle. r_{eq} was the equivalent hydraulic radius. During design, the self-driven sampling capability was enhanced by reducing θ and r_{eq} to avoid pulsation disturbances introduced by an external pump [14]. At the end of the main passage, a serpentine delay segment and a micro-column array buffer chamber were arranged to restrain the transient fluid flow fluctuation and bubble migration. Under laminar flow conditions, fluid transport obeys following.

$$Q = \frac{wh^3}{12\mu L}\Delta P \quad (7)$$

where Q was the volumetric flow rate. w was the channel width. h was the channel height. μ was the dynamic viscosity. L was the channel length. ΔP was the pressure drop along the channel. The main channel length was set to 18 - 25 mm to stabilize Q at 0.15 – 0.40 µL/min. The top of the detection chamber was covered with an 8 - 12 µm porous permeable membrane to block keratin debris and protein aggregates. The sampling delay was determined below.

$$\tau = \frac{V_c}{Q} \quad (8)$$

where τ was the sample renewal time constant. V_c was the volume of the detection chamber. By

ensuring thatV_c matched Q, the sensing interface maintained a stable fluid exchange rate under continuous wear conditions and reduced concentration tailing caused by residual old samples.

Wearable system integration and packaging

System integration took the modular architecture whereby it consisted of sensing patch, flexible interconnect, edge computing unit, and wireless transmission unit. These layers were laminated polyimide electrodes, polydimethylsiloxane microfluidic channels, and a medical grade pressure-sensitive adhesive to form the sensing patch. The error of interlayer alignment was maintained to less than 50 μm, coaxial control between the detection chamber and the working electrode [15]. Its flexible interconnect was based on an 18 μm copper foil/copper-clad polyimide flexible circuit board. The width of the critical signal lines was made to be 100 μm and 120 μm. To reduce weak current interference due to body motion and wireless coupling in the electrochemical front-end, a ring-shaped ground shielding layer was added in the electrochemical front-end. Anisotropic conductive adhesive by laying the sensing patch and the sensing module with an interface and low-modulus encapsulation resin was used to ensure that there was no mechanical failure when bending repeatedly. The edge computing module included a potentiostat front-end, analog-to-digital conversion, power management, and a Bluetooth Low Energy chip. The constant-potential control structure of three ops was selected with the range of bias of −0.2 - 0.8 V. The transimpedance amplifier used three-level feedback resistors of 100 kΩ, 1 MΩ, 10 MΩ, which enabled it to work with different current ranges. It used a 16-bit A/D converter with a sampling frequency of 50 – 200 Hz. When operated in the DPV mode, the system produced pulse scanning signals and simultaneously measured temperature and skin contact impedance as a measure of system stability and drift. The supply of power came from a 35 – 50 mAh flexible lithium-polymer battery with a regulated output of 3.3 V, and wireless transmission had a duty cycle of less than 5%. The packaging took a heterogeneous encapsulation scheme between fluid-permeable sensing areas and closed electronic areas. An 8 – 12 μm polyurethane membrane that was microporous was deposited to the sensing window to permit selective fluid permeation but exclude contaminants. The electronic module had been encased by 300 - 500 μm thermoplastic polyurethane to create a stress-relieve structure that allowed the reduction of deformation during attaching. The adhesive layer also had drainage/vent holes to avoid fluid retention and entrapping of air. The total size was managed to 35 mm × 25 mm × 3.5 mm. Sensing layer was disposable and the electronic module could be reused.

Electrochemical signal acquisition and feature extraction

Electrochemical signal acquisition and feature extraction were organized as a continuous workflow consisting of constant-potential excitation, transimpedance amplification, analog-to-digital conversion, digital preprocessing, and feature encoding. In this workflow, the potentiostat first applied the programmed excitation signal to the flexible three-electrode interface. The weak oxidation current generated by the target antiepileptic drug was then converted into a voltage signal through the transimpedance amplifier, digitized by the analog-to-digital conversion module, and subsequently processed by baseline correction, smoothing, and noise suppression before peak-related features were encoded for concentration inversion. A switching mode between DPV and time-resolved amperometry was used during continuous monitoring with DPV being applied to obtain the peak response of the target drug and time-resolved amperometry being used to monitor short-term concentration variation [16]. The differential pulse parameters were set as step potential (E_s) of 4 mV, pulse amplitude (E_p) of 25 mV, pulse width t_p of 50 ms, and scan cycle (T_{scan}) between 30 – 90 s. The time current bias potential was fixed in the vicinity of the characteristic oxidation potential, and the

sampling frequency was 100 Hz. The raw current signal was converted into a discrete sequence $i(k)$ after transimpedance amplification, where *k* was the sample point index. To suppress baseline drift and high-frequency noise, a combined sliding median filter and Savitzky-Golay smoothing method were applied as below.

$$i_c(k) = i(k) - \hat{\imath}_b(k) \quad (9)$$

where $i_c(k)$ was the corrected current. $\hat{\imath}_b(k)$ was the estimated baseline current, obtained *via* low-order polynomial fitting, which was used to remove the slowly varying background component [17]. During feature extraction, the main characteristic vector was composed of peak current, peak potential, peak area, peak half-width, and local kinetic slope. The peak area was calculated as follows.

$$A_p = \sum_{k=k_1}^{k_2} i_c(k)\Delta t \quad (10)$$

where A_p was the peak area. k_1 and k_2 were the peak boundary indices. Δt was the sampling time interval. This value was used to characterize the total electrochemical response per scanning cycle. The slope of the local rising segment was defined as below.

$$S = \frac{i_c(k_2) - i_c(k_1)}{t_{k_2} - t_{k_1}} \quad (11)$$

where *S* was the response slope. t_{k_1} and t_{k_2} were the corresponding time points. For the differential pulse sequence, the peak half-width, peak skewness, and peak position drift between adjacent scans were further extracted to form an extended feature set as below.

$$\boldsymbol{x} = [I_p, E_p, A_p, S, W_{1/2}, \Delta E_p]^T \quad (12)$$

where I_p was the peak current. E_p was the peak potential. $W_{1/2}$ was the half-width. ΔE_p was the peak position drift [18]. This vector was input directly into the following concentration inversion model and was combined with the simultaneous acquisition of temperature, contact resistance, and flow rate markers to form a multisource input matrix.

Concentration quantification model and calibration method

Concentration quantification employed a three-tier modeling approach consisting of segmented calibration + multivariate regression + body fluid correction. A standard series of 0.05 – 50 μmol/L was prepared, and calibration spectra were acquired under temperature, pH, and ionic strength conditions consistent with actual detection [19]. Peak current was dominant in the low concentration range, and combined correction with peak and half width was introduced in the high concentration range, so that the single characteristic was not distorted. The basic calibration equation was shown below.

$$\hat{C}_{\mathrm{f}} = \beta_0 + \sum_{j=1}^{m} \beta_j x_j \quad (13)$$

where $\hat{C}_f$ was the estimated drug concentration in body fluid. β_0 was the intercept term. β_j was the weight of the j-th feature. x_j was the corresponding input feature. m was the feature dimension. The parameter β_j was solved using weighted least squares, assigning higher weights to low-concentration samples to suppress the amplification of small errors near the therapeutic window [20]. To account for time lags and proportional shifts between body fluid and plasma drug concentrations, a personalized mapping model was further established as follows.

$$\hat{C}_{\mathrm{b}}(t) = \alpha_0 + \alpha_1 \hat{C}_{\mathrm{f}}(t-\tau) + \alpha_2 T + \alpha_3 \mathrm{pH} + \alpha_4 Zc \quad (14)$$

where $\hat{C}_b(t)$ was the estimated blood drug concentration at time *t*. τ was the response lag from body fluid to blood. T was skin temperature. pH was sample pH. Zc was skin contact impedance. α_i was the correction coefficient. During actual calibration, an *in vitro* static calibration was performed followed by

updating α_i and τ using a small number of paired samples. The model training objective function was defined as follows.

$$L = \frac{1}{N}\sum_{i=1}^{N}\left(C_{\text{ref,i}} - \hat{C}_{\text{b,i}}\right)^2 + \lambda\left\|\beta\right\|_2^2 \quad (15)$$

where *N* was the number of samples. $C_{ref,i}$ was the reference concentration. λ was the regularization coefficient. $\|\beta\|_2^2$ was the parameter penalty term. Recursive updating was used in the on-line operating stage, which only adjusted the intercept and environment compensation parameters, while freezing the major feature weighted to assure the steady output of the model.

Signal drift compensation and anti-interference algorithm

The drift compensation and anti-interference algorithm was based on four steps including condition monitor, baseline separation, dynamic correction, and abnormal rejection. In the case of continuous wear, the contamination of the electrode, the regeneration of the functional layer, the fluctuation of temperature, and the deformation of the skin could result in the gradual change of the baseline. The sudden change in the rate of perspiration, the intrusion of the air, and the contact interference appeared as abrupt spike noise. The acquisition end simultaneously input current sequences *i*(*k*), temperature *T*(*k*), contact impedance *Zc*(*k*), and sampling flow rate *Q*(*k*). The drift observation was constructed as below.

$$d(k) = i(k) - i_{ref} \quad (16)$$

where *d*(*k*) was the drift offset. i_{ref} was the reference current extrapolated from the most recent stable window. The stable window length was set to 120 – 180 s to limit the inclusion of short-period drug fluctuations in the baseline term. State-space compensation was used for slow-varying drift. Let the true response be *s*(*k*) and the baseline drift be *b*(*k*), then the observation model was written as follows.

$$i(k) = s(k) + b(k) + v(k) \quad (17)$$

$$b(k) = b(k-1) + w(k) \quad (18)$$

where *v*(*k*) was the measurement noise. *w*(*k*) was the drift state disturbance. For online estimation, a first-order Kalman recursive update $\hat{b}(k)$ was used as follows.

$$i_{\text{corr}}(k) = i(k) - \hat{b}(k) - \gamma_T \Delta T(k) - \gamma_Z \Delta Z_c(k) \quad (19)$$

where $i_{corr}(k)$ was the corrected current. γ_T and γ_Z were the sensitivity coefficients for temperature and contact resistance, respectively. $\Delta T(k)$ and $\Delta Z_c(k)$ were the offsets relative to the calibration conditions. These values were obtained by piecewise fitting during the preliminary experiments and were updated in small increments during the online phase. Burst disturbance discrimination employed a combination of residual threshold and local morphology. The residual was defined as follows.

$$r(k) = i_{\text{corr}}(k) - \hat{s}(k) \quad (20)$$

where $\hat{s}(k)$ was the local expected response obtained by median filtering within a short window.

$$G(k) = \frac{i_{\text{corr}}(k) - i_{\text{corr}}(k-1)}{\Delta t} \quad (21)$$

When $|r(k)| > \eta\sigma_r$ and the local slope exceeded a preset threshold, that point was marked as an anomaly. η was set to 3.0 – 3.5. σ_r was the residual standard deviation. Δt was the sampling interval. Anomalous segments were reconstructed using cubic spline interpolation, and confidence labels were attached to the reconstructed segments to prevent direct entry into the concentration update phase. From the compensated signal, the final output characteristic vector was calculated and linked to the regression model. The concentration update was only triggered if the confidence level was above the set threshold.

Experimental setup and conditions

The sensor patch was fabricated under cleanroom conditions using the integrated flexible electrode and microfluidic structure described above. During fabrication, the polyimide film (DuPont, Wilmington, Delaware, USA) was rinsed with ethanol and deionized water, dried with nitrogen, treated for 60 s using a plasma cleaner (Diener Electronic GmbH, Ebhausen, Baden-Württemberg, Germany), and coated with 5 nm Ti and 120 nm Au films using a magnetron sputtering system (Shenyang Kejing Auto-instrument Co., Ltd., Shenyang, Liaoning, China) to form the three-electrode pattern. Then, 4 μL rGO dispersion (XFNANO Materials Tech Co., Ltd., Nanjing, Jiangsu, China) was drop-coated on the working electrode and dried at 40°C for 30 min. Electrochemical measurements were performed using a PalmSens4 portable potentiostat (PalmSens BV, Houten, Utrecht, Netherlands) and an LSP01-1C syringe pump (Longer Precision Pump Co., Ltd., Baoding, Hebei, China). Carbamazepine and lamotrigine reference standards (Aladdin Biochemical Technology Co., Ltd., Shanghai, China) were used as representative antiepileptic drugs. Stock solutions were prepared first and then diluted with pH 7.0 PBS to 0.05, 0.5, 1, 5, 10, 50, and 80 μmol/L. Each solution was introduced at 0.7 – 1.0 μL/min and stabilized for 5 min before triplicate DPV and chronocoulometry tests, followed by interference testing, 12 h stability evaluation, and comparison using an Agilent 1260 Infinity II high-performance liquid chromatography (HPLC) system (Agilent, Santa Clara, California, USA). Key fabrication parameters were controlled during sensor preparation to ensure stable electrode performance and microfluidic mass transfer. During conductive-layer preparation, the Au film thickness was controlled at 110 – 130 nm to reduce interfacial resistance. For rGO modification, 3 – 5 μL of dispersion was drop-coated to form a continuous conductive network. Gold nanoparticle deposition was performed for 150 – 200 s to regulate particle size and distribution. The imprinting layer was prepared with a polymerization charge of 0.9 – 1.1 mC to balance molecular recognition and electron conduction. The microfluidic channel width and height were maintained at 140 – 160 μm and 40 – 60 μm, respectively, to ensure stable laminar flow, while the sampling flow rate was controlled at 0.7 – 1.0 μL/min to maintain consistent mass transfer. These parameters were used to maintain reproducible electrode modification, stable laminar flow, and consistent interfacial mass transfer during subsequent electrochemical testing.

Detection performance evaluation

Under the above experimental conditions, antiepileptic drug standard solutions at different concentrations were tested systematically to evaluate sensor sensitivity, repeatability, and linearity. Carbamazepine and lamotrigine standard stock solutions were introduced into the microfluidic channel, respectively. After stabilization, DPV was performed in triplicate for each concentration level. The peak current, sensitivity, and relative standard deviation (RSD) were calculated for subsequent detection-performance analysis.

Interference resistance evaluation

To evaluate biofluid interference, uric acid, ascorbic acid, D-glucose, and sodium lactate (Sigma-Aldrich, St. Louis, Missouri, USA) were used as representative interferents. The interferent solutions were prepared using pH 7.0 PBS and mixed with 10 μmol/L carbamazepine or lamotrigine standard solution. Single-interferent and mixed-interferent samples were introduced into the microfluidic channel at 0.7 – 1.0 μL/min. After 5 min stabilization, DPV measurements were performed in triplicate using PalmSens4 portable potentiostat and LSP01-1C syringe pump. Response deviation was calculated against the target-drug solution without interferents.

HPLC reference comparison

To verify detection accuracy, 25 laboratory-prepared simulated body-fluid samples were used for comparison between the wearable sensing system and HPLC. Carbamazepine and lamotrigine standards were diluted with pH 7.0 PBS to prepare 25 concentration-varied spiked

Table 1. Statistical analysis of detection performance.

Concentration (μmol/L)	Peak Current (μA)	Sensitivity	Relative standard deviation (RSD) (%)
0.05	0.23	4.6	4.2
0.5	2.12	4.24	3.7
1	4.18	4.18	3.3
5	20.1	4.02	2.9
10	39.2	3.92	2.6
50	148.6	2.97	2.3
80	181.2	2.27	2.1

samples covering 0.05 – 80 μmol/L. Each sample was tested by the wearable sensor and then filtered through a 0.22 μm membrane before HPLC analysis. HPLC measurements were performed with a C18 column (Agilent Technologies, Santa Clara, California, USA) at 30°C with acetonitrile/PBS as the mobile phase at a flow rate of 1.0 mL/min, an injection volume of 10 μL, and ultraviolet detection at the characteristic absorption wavelength of each analyte.

Results and discussion

Detection performance analysis

The detection performance results demonstrated that the peak current increased with drug concentration, rising from 0.23 μA at 0.05 μmol/L to 181.2 μA at 80 μmol/L. In the low concentration range of 0.05 – 10 μmol/L, the current response showed good linearity with a sensitivity of approximately 4.0 μA per μmol/L and a relative standard deviation below 4%, indicating stable and repeatable trace-level detection. At higher concentrations, the growth rate of the current response slowed, and the sensitivity decreased to approximately 2.4 μA per μmol/L, which might be attributed to gradual saturation of interfacial adsorption sites and increased diffusion-mass transfer resistance (Table 1). The DPV curves under different concentrations exhibited a well-defined single oxidation peak near 0.60 V with no obvious peak shift (Figure 4). The result suggested that the electrode reaction remained stable and was not significantly affected by side reactions. The peak current increased progressively with concentration, while the peak shape remained symmetrical without obvious broadening or distortion, indicating stable electron transport and mass-transfer behavior of the functional layer across the tested range.

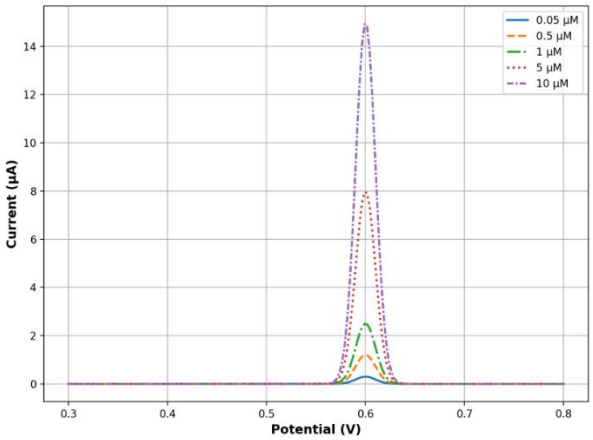

Figure 4. DPV current response curves at different concentrations.

The peak current exhibited a strong linear relationship with drug concentration in the low-concentration range with a correlation coefficient above 0.995 and a detection limit of approximately 0.03 μmol/L. At higher concentrations, the calibration curve gradually deviated from linearity because of interfacial adsorption-site saturation and increased diffusion-layer resistance (Figure 5). Overall, the sensor demonstrated favorable quantitative performance and dynamic response characteristics within the clinically relevant therapeutic concentration range.

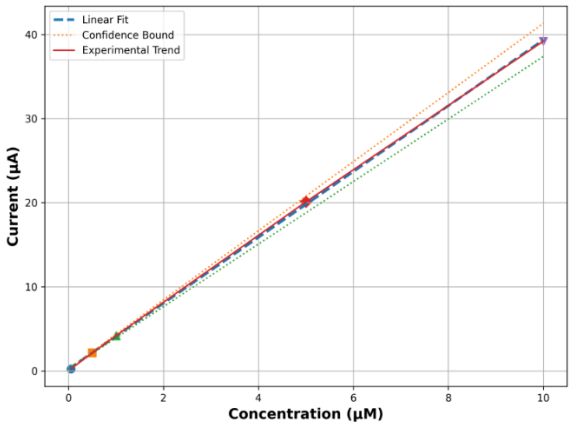

Figure 5. Linear detection range and fitting results.

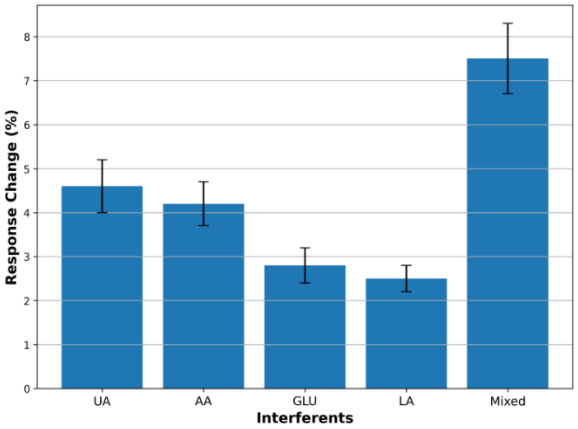

Figure 6. Response variation under conditions of coexisting interferents.

Interference resistance and stability

The interference resistance results showed that, under single-interferent conditions, the current response deviation remained below 5%. The highest deviations were observed for uric acid and ascorbic acid at 4.6% and 4.2% respectively, mainly because these electroactive molecules had oxidation potential close to that of the target drug signal. Under mixed interferent conditions, the total response deviation was 7.5%, which was much lower than the typical 18% deviation observed for unmodified electrodes, indicating that the molecularly imprinted layer provided strong selective recognition of the target molecules (Figure 6). The results indicated that the imprinted layer effectively blocked nonspecific adsorption through structural matching and local charge screening, while its porous structure provided mass-transfer pathways for target molecules and improved selectivity. The stability test showed that the original current signal decreased by approximately 5% during 12 h of continuous operation, whereas signal drift compensation reduced the variation to within ±2%. This result indicated that the system maintained stable monitoring performance under simulated complex body-fluid and dynamic wearing conditions.

Comparison with standard methods

The HPLC reference comparison results obtained from 25 laboratory prepared simulated body fluid spiked samples showed good agreement between the wearable sensing system and the standard method. The concentrations measured by the wearable sensor were strongly correlated with those obtained by HPLC with a correlation coefficient of 0.987 (Figure 7). Most data points were distributed close to the fitted line, indicating that the proposed system maintained reliable quantitative consistency with the reference method across the tested concentration range. Slightly higher sensor responses at low concentrations might be attributed to the enrichment effect of the molecularly imprinted layer, which enhanced the local electrochemical signal of target molecules.

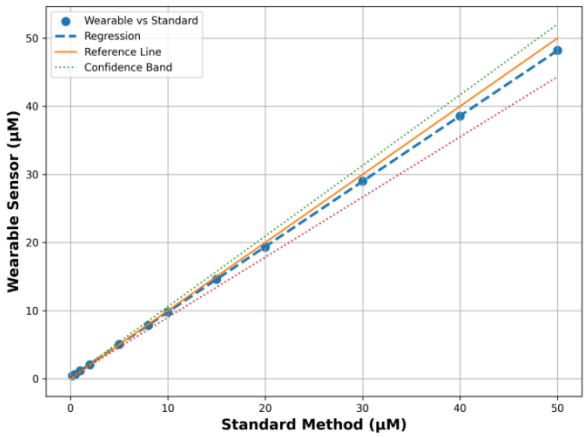

Figure 7. Correlation plot between wearable detection and the standard method.

The comparison results showed that most relative errors between the two methods were within ±8%, more than 70% of the samples showed errors below 5%, and the maximum error was approximately 10%. The error distribution was slightly positively biased, suggesting limited signal amplification in the low-concentration range. After temperature correction and individualized calibration were introduced, quantitative stability was improved, and the standard deviation decreased from 6.3% to 3.9% (Figure 8). These results indicated that the dynamic correction model effectively reduced deviations caused by body-fluid response delay, environmental fluctuation, and interfacial signal drift.

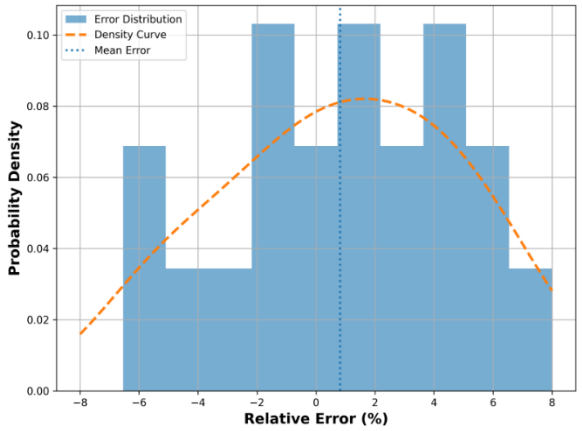

Figure 8. Error distribution plots for the two methods.

Overall, the wearable electrochemical sensor combining flexible electrodes, microfluidic sampling, molecularly imprinted recognition, multi-parameter signal acquisition, and dynamic correction achieved sensitive plasma-concentration-related detection under low concentration and interference prone conditions. The strong linear response within the therapeutic concentration range, reproducible current output, controlled interference deviation, and high consistency with the HPLC reference method jointly demonstrated the feasibility of the proposed sensing strategy for real-time antiepileptic drug monitoring and precision medicine-oriented dose adjustment. Nevertheless, several limitations should be considered when interpreting these results. Individual differences might still affect the mapping relationship between body fluid signals and actual plasma concentrations, and the long-term stability and biocompatibility of the functional layer under continuous wearing conditions required further validation. In addition, the coupling mechanism by which temperature, pH, contact impedance, and sampling flow fluctuation influence electrochemical drift had not yet been fully quantified. Future work should focus on individualized calibration models, more stable functional materials, multimodal sensing integration, and machine learning assisted concentration prediction, thereby improving the robustness of wearable precision medication monitoring and extending the system toward simultaneous detection of multiple antiepileptic drugs.

References

1. Mobed A, Shirafkan M, Charsouei S, Sadeghzadeh J, Ahmadalipour A. 2022. Biosensor technology for anti-epileptic drugs. Clin Chim Acta. 533:175-182.
2. Habtamu M, Tolosa K, Abera K, Demissie L, Samuel S, Temesgen Y, *et al*. 2023. A novel wearable device for automated real-time detection of epileptic seizures. BMC Biomed Eng. 5(1):7.
3. Bian S, Zhu B, Rong G, Sawan M. 2021. Towards wearable and implantable continuous drug monitoring: A review. J Pharm Anal. 11(1):1-14.
4. Liu Y, Li J, Xiao S, Liu Y, Bai M, Gong L, *et al*. 2023. Revolutionizing precision medicine: Exploring wearable sensors for therapeutic drug monitoring and personalized therapy. Biosensors (Basel). 13(7):726.
5. Ganesan M, Devi RK, Wang CL, Lin YC, Lin WC, Lin SF, *et al*. 2025. From lab to body: Advanced electrochemical biosensors for illicit drug detection via nanomaterials, AI, and wearable tech. ACS Sens. 10(12):9153-9182.
6. Pollard TD, Ong JJ, Goyanes A, Orlu M, Gaisford S, Elbadawi M, *et al*. 2021. Electrochemical biosensors: A nexus for precision medicine. Drug Discov Today. 26(1):69-79.
7. Fu E, Khederlou K, Lefevre N, Ramsey SA, Johnston ML, Wentland L. 2023. Progress on electrochemical sensing of pharmaceutical drugs in complex biofluids. Chemosensors. 11(8):467.
8. Zheng Z, Zhu R, Peng I, Xu Z, Jiang Y. 2024. Wearable and implantable biosensors: Mechanisms and applications in

closed-loop therapeutic systems. J Mater Chem B. 12(35):8577-8604.

9. Khadka B, Lee B, Kim KT. 2023. Drug delivery systems for personal healthcare *via* smart wearable patch systems. Biomolecules. 13(6):929.
10. Brinkmann BH, Karoly PJ, Nurse ES, Dumanis SB, Nasseri M, Viana PF, *et al*. 2021. Seizure diaries and forecasting with wearables: Epilepsy monitoring outside the clinic. Front Neurol. 12:690404.
11. Paci MM, Saha T, Djassemi O, Wu S, Chua CYX, Wang J, *et al*. 2025. Smart closed-loop drug delivery systems. Nat Rev Bioeng. 3(10):816-834.
12. Li Z, Wang Y, Zhang R, Liu Z, Chang Z, Deng Y, *et al*. 2024. Microneedles-based theranostic platform: From the past to the future. ACS Nano. 18(35):23876-23893.
13. Duan H, Peng S, He S, Tang SY, Goda K, Wang CH, *et al*. 2025. Wearable electrochemical biosensors for advanced healthcare monitoring. Adv Sci (Weinh). 12(2):e2411433.
14. Xu L, Zhou Z, Fan M, Fang X. 2023. Advances in wearable flexible electrochemical sensors for sweat monitoring: A mini-review. Int J Electrochem Sci. 18(1):13-19.
15. Xu L, Yang Y, Mao Y, Li Z. 2022. Self-powerbility in electrical stimulation drug delivery system. Adv Mater Technol. 7(2):2100055.
16. Guo L, Lee HK, Oh S, Koirala GR, Kim TI. 2025. Smart bioelectronics for real-time diagnosis and therapy of body organ functions. ACS Sens. 10(5):3239-3273.
17. Rajee MV, Vallisuseela R, Princy SSL, Varsha MR: Smart drug delivery through Internet of Things: Current progress and future challenges. In Connected Diagnoses: IoT, Healthcare, and Digital Forensics. 1st edition. Edited by Kaushik K, Chaudhary A. Amsterdam: Elsevier. 2026:57-70.
18. Sajeevan A, Sukumaran RA, Panicker LR, Kotagiri YG. 2025. Trends in ready-to-use portable electrochemical sensing devices for healthcare diagnosis. Microchim Acta. 192(2):80.
19. Shalannanda W, Satriawan A, Nurrajab MF, Ayulestari ACH, Safitri DA, Nabila FA, *et al*. 2023. Biosensors for therapeutic drug monitoring: A review. F1000Res. 12:171.
20. Booth MA, Gowers SAN, Leong CL, Rogers ML, Samper IC, Wickham AP, *et al*. 2018. Chemical monitoring in clinical settings: Recent developments toward real-time chemical monitoring of patients. Anal Chem. 90(1):2-18.